International Journal for Multidisciplinary Research (IJFMR)
E-ISSN: 2582-2160 ● Website: www.ijfmr.com ● Email: editor@ijfmr.com

Structural I-V Characterization of Spray Pyrolysis Deposited Al^{3+}, Gd^{3+} Co-Doped Nickel Ferrite Thin Film

Vikas U. Magar[1], Sagar Rathod[2], Sudarshan Tapsale[3], M. K. Babrekar[4], K.M. Jadhav[5]

[1,2]Department of Physics, Deogiri College, Chhatrapati Sambhajinagar-431001, (MS), India
[3]Department of Chemistry, Shree Chhatrapati Shivaji College, Omerga, Dharashiv- 413606 (MS), India
[4] Department of Physics, Indraraj Arts, Commerce and Science College, Sillod-431112 (MS), India
[5]School of Basic and Applied Science, MGM University, Chhatrapati Sambhajinagar-431003, (MS), India

Abstract

In this paper, we report the preparation of nanocrystalline thin films of Nickel aluminate and Gadolinium spinel ferrite, having the chemical formula $NiFe_{2-x}Al_xGd_xO_4$, where Al^{3+} and Gd^{3+} vary from 0.00 to 0.02 and 0.04, respectively, with a rise of 0.02, using the well-known spray pyrolysis deposition method. The thin films were grown and deposited on ultrasonically clean glass substrates. The X-ray diffraction pattern shows the orientation of various diffraction peaks at (220), (311), (222), (400), (422), (511), and (540). The occurrence of this diffraction peak suggests the formation of a single-phase compound, as there are no extra diffraction peaks in the XRD pattern other than the cubic spinel phase. The crystallite size, deduced from the Debye-Scherrer equation, varies in the range of 17 nm to 15 nm. The Lattice parameter was found to decrease with the doping of Al^{3+} and Gd^{3+} ions. FTIR spectra show the absorption bands close to the 400 cm^{-1} and 600 cm^{-1} wave numbers, which are attributed to stretching vibrations of the metal oxygen bond. The ohmic nature of the prepared thin film was confirmed through I-V characteristics.

Keywords: Thin Film, Nickel ferrite, Spray pyrolysis, lattice constant, I-V

1. Introduction

The ferrite-based oxide magnetic materials have been the subject of thorough research for more than seven decades due to their diverse and technologically important properties[1]. Their unusual electrical, optical, dielectric, catalytic, and magnetic characteristics allow their use across a broad spectrum of applications, including storage materials, micro-devices, and gas sensors, water-splitting reactions, and electromagnetic wave absorption[2]. The ferrite films are well used as magnetic core materials with low iron loss, opto-magnetic devices, and vertical recording magnetic material in surface magnetism studies[3]. The ferrites can be confidential into three main families: spinel ferrites, cubic garnets, and hexagonal ferrites[4]. Among these, spinel ferrites represent the most commonly studied and technologically important class due to their outstanding combination of magnetic and electrical properties[5]. The ferrites with the general chemical formula MFe_2O_4 (M = divalent metal) show the cubic spinel structure[6]. It contains two atomic

sites for divalent metal ions and trivalent Fe ions, namely, the tetrahedral (A) site and the octahedral (B) site[7]. Depending on the distribution of metal cations over these sites, spinel ferrites can adopt normal, inverse, or diverse spinel structures[8]. The electrical conductivity, magnetic ordering, dielectric behaviour, and optical response of ferrites are strongly ruled by this cation distribution, which in turn depends on ionic radius, valence state, and synthesis conditions[9].

It is well conventional that the essential physical properties of ferrites are highly complex in the method of synthesis[10]. The bulk ferrites are conservatively produced by solid-state ceramic methods, which typically need high processing temperatures[11]. In divergence, nanocrystalline ferrites can be obtained through low-temperature wet-chemical routes such as sol–gel, co-precipitation, hydrothermal, or combustion synthesis[12]. For device-level integration, ferrites are frequently fabricated in thin-film form, which provides not only a large surface-to-volume ratio but also better-quality compatibility with microelectronic architectures.

Currently, ferrite thin films have attracted considerable attention due to their unusual magnetic anisotropy, enhanced dielectric properties, and tunable optical response at the nanoscale[13]. Thin-film deposition can be attained through a variety of techniques, broadly categorised into physical and chemical approaches[14]. Physical methods include pulsed laser deposition (PLD), RF sputtering, and thermal evaporation, which generally provide high-quality films but require exclusive equipment[15]. Alternatively, chemical methods such as sol–gel processing, electrodeposition, chemical vapour deposition, and spray pyrolysis offer cost-effective and scalable routes for thin-film fabrication[14].

Among these, spray pyrolysis has emerged as one of the most versatile and widely used techniques for preparing ferrite thin films[16]. The method is relatively simple, inexpensive, and adaptable for large-area deposition on substrates such as glass, quartz, or silicon[17]. Several processing parameters—such as spray rate, carrier gas pressure, precursor concentration, nozzle-to-substrate distance, substrate temperature, and post-deposition annealing—critically influence the structural, morphological, and functional characteristics of the subsequent films[18]. Owing to its flexibility, spray pyrolysis has been extensively employed to synthesize spinel ferrite thin films with tailored microstructure and properties for diverse applications, ranging from optoelectronic devices to electromagnetic interference shielding materials[19].

Thus, by careful optimization of synthesis routes, cation substitution, and thin-film processing parameters, spinel ferrites continue to offer immense potential for next-generation multifunctional materials and devices[20].

In the present study, nickel ferrite ($NiFe_2O_4$), a prominent member of the spinel ferrite family, has been selected in its pure form as well as in Al^{3+} and Gd^{3+} co-doped compositions for a detailed study of their functional properties. Thin films of $NiFe_{2-x}Al_xGd_xO_4$ were manufactured using the spray pyrolysis technique, where the deposition parameters such as substrate temperature, precursor concentration, and spray rate were carefully improved to achieve uniform, adherent, and nanocrystalline films. The synthesized samples were subjected to comprehensive characterization to elucidate their structural, Raman vibrational, electrical, and (I–V) properties. The structural analysis offers insight into the crystallinity and lattice modifications induced by co-doping, whereas Raman spectroscopy confirms local vibrational modes associated with the spinel structure. Current–voltage characteristics were examined to assess the nature of electrical transport. The systematic correlation between dopant-induced modifications and the observed physical properties highlights the potential of Al^{3+} and Gd^{3+} co-doped nickel ferrite thin films for multifunctional device applications.

2. Materials and Methods

2.1 Materials

The AR grade nickel nitrate hexahydrate (Ni $(NO_3)_2.6H_2O$), aluminium nitrate nonahydrate (Al $(NO_3)_3.9H_2O$), gadolinium nitrate nonahydrate (Gd $(NO_3)_3.9H_2O$), and ferric nitrate nonahydrate (Fe $(NO_3)_3.9H_2O$) were used as starting materials. The glass substrates were carefully dipped in chromic acid for 45 min. These glass slides were cleaned in the ultrasonic bath for 25-30 min and used as a glass substrate.

2.2 Synthesis

Thin films of $NiFe_{2-x}Al_xGd_xO_4$ (x = 0.00, 0.02, and 0.04) were deposited on optically transparent glass substrates of dimensions 75 mm × 25 mm × 1.35 mm by employing the spray pyrolysis method. High-purity precursor salts (~99.98%), namely nickel nitrate hexahydrate (Ni $(NO_3)_2.6H_2O$), aluminium nitrate nonahydrate (Al $(NO_3)_3.9H_2O$), gadolinium nitrate nonahydrate (Gd $(NO_3)_3.9H_2O$), and ferric nitrate nonahydrate (Fe $(NO_3)_3.9H_2O$), served as starting materials. Each nitrate compound was first dissolved individually in deionised water to prepare 0.1 M solutions of Ni^{2+}, Al^{3+}, Gd^{3+}, and Fe^{3+} ions. These solutions were then combined in such a manner that the cationic proportion of Ni^{2+} (Fe^{3+} + Al^{3+} + Gd^{3+}) remained 1:2, in accordance with the stoichiometry of $NiFe_{2-x}Al_xGd_xO_4$. Nickel nitrate provided the main cationic source, while ferric nitrate, along with controlled quantities of aluminium and gadolinium nitrates, constituted the secondary fraction, thereby ensuring the required chemical composition of the final spray solution. The homogeneous precursor solution was atomised through a spray nozzle and directed onto glass substrates maintained at ~385 °C. The spraying pressure was maintained at approximately 0.25 Pa to ensure uniform film growth. Following each spray burst, the substrate temperature showed a slight decrease and typically required 2–6 minutes to return to the present value, which was regulated by a digital temperature controller. Other deposition parameters, including spray rate, pressure, and nozzle-to-substrate distance, were optimised and are presented in **Table. 1** After the deposition process, the substrates were kept at the same temperature for 20–25 minutes to ensure proper film formation and then allowed to cool gradually to room temperature. To improve crystallinity and remove any residual moisture or unwanted phases, the as-prepared films were annealed at 550 °C for 4 hours.

2.3 Growth and deposition of $NiFe_{2-x}Al_xGd_xO_4$ thin film

In this work, undoped nickel ferrite ($NiFe_2O_4$) with a normal spinel structure, as well as Al^{3+} and Gd^{3+} substituted nickel ferrite ($NiFe_{2-x}Al_xGd_xO_4$), were deposited on cleaned glass substrates via the spray pyrolysis technique. A schematic of the process is illustrated in **Figure. 1** Precursor solutions of nickel nitrate, ferric nitrate, and aluminium nitrate were atomised using compressed air and delivered onto substrates preheated to approximately 550 °C. Upon impact, the aerosol droplets decomposed thermally, giving rise to thin, adherent ferrite films.

3. Characterizations

To examine the structural, vibrational, and electrical characteristics of the Al^{3+} and Gd^{3+} substituted nickel ferrite thin films, a variety of analytical techniques were employed. Structural analysis was carried out using a BRUKER D8 Advance X-ray diffractometer with Cu-Kα radiation, within the 2θ scanning range of 20°–80°.

Table 1. Experimental parameters of $NiFe_{2-x}Al_xGd_xO_4$ (x = 0.00, 0.02, and 0.04) thin Films by spray pyrolysis deposition techniques.

Parameters	Specification
Molarity proportion	1:2
Volume proportion	1:2
Dimensions Cleaned glass	(75 mm × 25 mm × 1.35 mm)
Nozzle to substrate distance	29 cm
Spray rate	2-4 ml/min
Spray pressure	0.25 Pa
Substrate temperature	385°C
Annealing temperature and time	550°C for 4 h

The vibrational modes of the films were investigated through Fourier Transform Infrared Spectroscopy (FTIR) using a JASCO FT-IR 6600 spectrophotometer, covering the spectral window from 4000 to 400 cm^{-1}. Raman scattering measurements were obtained at room temperature with the STR-500 Micro-Raman spectrometer (Japan). Film thickness for the doped samples was estimated using the width difference method.

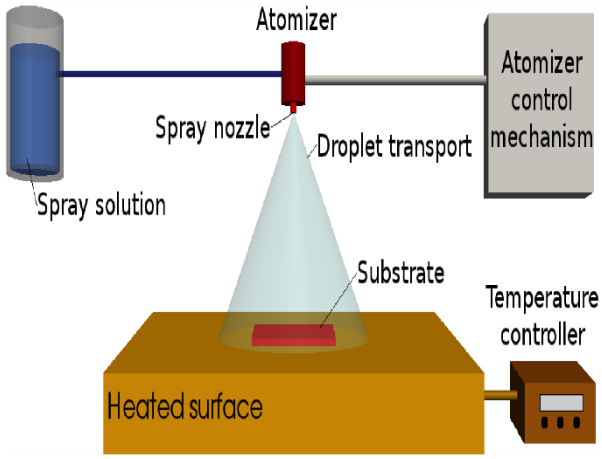

Fig.1. Block Diagram of the deposition of thin film onto a glass substrate.

4. Results and Discussion

4.1 X-ray Diffraction

Thickness of the Film is a key parameter since it significantly affects the structural, morphological, optical, and electrical behaviour of thin films, thereby influencing their potential applications[21]. In this study, the thickness of $NiFe_{2-x}Al_xGd_xO_4$ thin films was determined using the conventional weight difference method. The weights of both the uncoated glass substrate and the substrate after film deposition were measured with a single-pan analytical balance having an accuracy of ±0.01 mg[22]. Thickness values were then obtained using the standard relation, and the calculated results are presented in **Table. 3**

$$t = \frac{\delta m}{A\rho} \quad (1)$$

where δ delta is the density of the material, mmm is the mass of the film, and A is the surface area of the substrate.

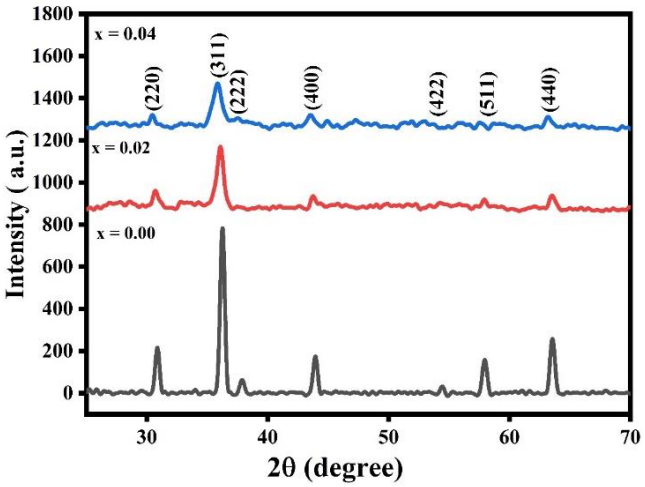

Figure 2. X-ray diffraction pattern of $NiFe_{2-x}Al_xGd_xO_4$ (x = 0.00, 0.02, and 0.04) thin films.

Table 2. Values of Bragg's angle (2θ), Miller indices (hkl), Intensity (I), (I/Io) relative intensity and Interplanar spacing (d) of $NiFe_{2-x}Al_xGd_xO_4$ (x = 0.00, 0.02, and 0.04) thin films.

	x = 0.00			
Bragg's angle (2θ)	**Miller indices (h k l)**	**Intensity (a. u.)**	**I/Io**	**Interplanar spacing (d)Å**
30.76	220	1452.8	37.3	2.9036
36.12	311	3892.5	100.0	2.4841
37.24	222	449.1	11.5	2.4119
43.87	400	916.8	23.6	2.0616
53.31	422	983.1	25.3	1.7166
57.21	511	1061.5	27.3	1.6085
62.15	440	1326.2	34.1	1.4920

The room-temperature X-ray diffraction (XRD) patterns of Al^{3+} and Gd^{3+} co-doped nickel ferrite $NiFe_{2-x}Al_xGd_xO_4$ thin films are presented in **Figure 2.** The diffraction peaks are indexed to the (220), (311), (222), (400), (422), (511), and (440) planes, consistent with Bragg's law[23]. The presence of sharp yet slightly broadened reflections indicates the nanocrystalline nature of the films[24]. The obtained patterns exhibit good agreement with previously reported spinel ferrites and correspond well with the standard JCPDS card no. 08-0234[25]. The absence of secondary peaks confirms the formation of a single-phase cubic spinel structure. A detailed analysis of the diffraction data was conducted to determine structural parameters, including the lattice constant, unit cell volume, and X-ray density. These values, calculated using standard crystallographic relations, are summarised in **Table. 2** The lattice constant (a) was evaluated using the relation,

$$a^2 = \frac{\lambda^2(h^2+k^2+l^2)}{4sin^2\theta} \quad (2)$$

The lattice parameter of undoped nickel ferrite was found to be in close agreement with the values reported in earlier studies. A systematic increase in the lattice constant was observed upon substitution with Gd^{3+} ions. This variation can be understood in terms of the difference in ionic radii between the dopant and host cations. In the present case, Fe^{3+} ions at the octahedral sites are progressively replaced by Al^{3+} and Gd^{3+} ions. Since the ionic radii of Al^{3+} (0.51 Å) and Gd^{3+} (0.93 Å) differ from that of Fe^{3+} (0.67 Å), the incorporation of the larger Gd^{3+} ions lead to an expansion of the lattice.

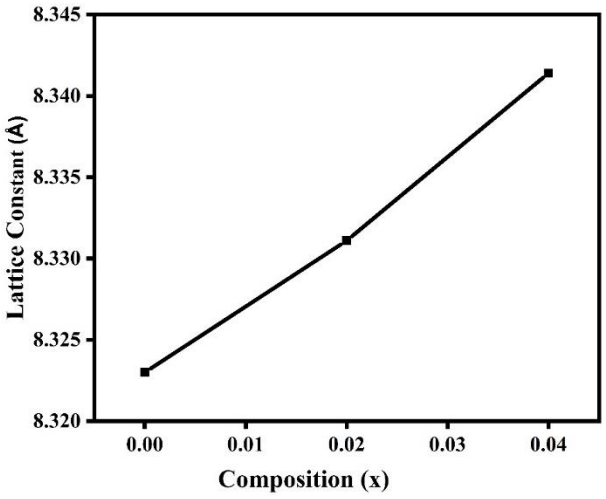

Figure 3. Lattice constant vs composition (x) for $NiFe_{2-x}Al_xGd_xO_4$ (x = 0.00, 0.02, and 0.04) thin films.

Consequently, the unit cell volume (V), evaluated from the lattice constant (a), also shows a gradual increase with Gd^{3+} concentration, as summarised in **Table. 3** Furthermore, the X-ray density (ρ_x) was determined using the standard relation[26],

$$(\rho_x) = \frac{8M}{N_A a^3} \quad (3)$$

where *Z* is the number of formula units per unit cell, *M* is the molecular weight, *N_A* is Avogadro's number, and *a* is the lattice constant.

The molecular weight of the compound is denoted by *m*, the lattice parameter by *a*, and N_a represents Avogadro's number. As presented in the Table, the X-ray density exhibits a decreasing tendency with progressive substitution of Gd^{3+} ions. This reduction can be correlated with the increase in dopant

concentration (x). The average crystallite size was determined using the Scherrer relation, expressed in the equation[27],

$$D = \frac{0.9\lambda}{\beta cos\theta} \quad (4)$$

Where λ is the wavelength, θ is Bragg's angle of diffraction and β is the FWHM (Full width at half maxima). The obtained values are listed in the **Table. 3**

Table. 3 Values of thickness (t), crystallite size (D) by Debye Scherrer, crystallite size (D) by W-H plot, lattice constant(a), X-ray density (d_x), and Volume (V) of $NiFe_{2-x}Al_xGd_xO_4$ (x = 0.00, 0.02, and 0.04) thin films.

Composition x	t (nm)	D (nm) by Debye-Scherrer	D (nm) by W-H	a (Å)	d_x (g/cm^3)	Volume (Å)^3
0.00	239	9	17	8.3230	5.4056	576.5
0.02	222	13	17	8.3311	5.4343	578.2
0.04	257	15	15	8.3414	5.4437	580.4

The microstructure parameters are calculated using the following relation[28],

$$LS = \frac{\beta}{4tan\theta} \quad (5)$$

$$\varepsilon = \frac{\beta cos\theta}{4} \quad (6)$$

$$\delta = \frac{1}{D^2} \quad (7)$$

$$SF = \frac{2\pi^2}{45\sqrt{3}tan\theta} \quad (8)$$

Table. 4 presents the calculated structural parameters of the prepared thin films. Lattice strain provides insight into the extent of distortion within the crystal lattice, which can originate from thermal expansion, point defects, dislocations, surface stress, and other intrinsic or extrinsic factors[29]. An increase in lattice strain with progressive Al^{3+} and Gd^{3+} co-doping indicates enhanced lattice distortion, consistent with the substitution of cations of different ionic radii into the host matrix. The estimation of microstrain further supports this observation, as it reflects the degree of local lattice deformation. As summarised in Table 4, the microstrain values are relatively low but exhibit a systematic increase with higher Al^{3+} and Gd^{3+} concentrations, suggesting a uniform distribution of dopant ions and minimal compositional inhomogeneity in the synthesised films.

Dislocation density, which quantifies the density of linear imperfections in the lattice, also shows a noticeable increase with Gd^{3+} incorporation[27]. This trend implies the generation of additional crystal defects and localised distortions, which could play a role in modifying the mechanical stability and electronic behaviour of the thin films[30]. In contrast, the stacking fault probability remains nearly unchanged across all doping levels, signifying that the overall stacking sequence of atomic planes is preserved despite the introduction of dopants[31]. Overall, the microstructural analysis reveals that Al^{3+} and Gd^{3+} co-doping induces measurable lattice strain, higher macrostrain, and increased dislocation density, while leaving the stacking fault probability almost unaffected. These findings highlight the

delicate balance between structural distortion and lattice stability in co-doped nickel ferrite thin films, which may strongly influence their functional properties, such as electrical conductivity, optical response, and magnetic behaviour.

Table. 4 Values of Lattice strain (LS), micro strain (ε), Dislocation density (δ), Stacking fault (SF) for XRD patterns of $NiFe_{2-x}Al_xGd_xO_4$ (x = 0.00, 0.02 and 0.04) thin films.

x	LS	ε (*10^{-}	δ (*10^{16} lines/m^{-2})	SF (*10^{-2})
0.00	3.5750	1.9201	3.0709	0.0556
0.02	4.7036	5.2667	5.2667	0.0554
0.04	4.0210	2.1959	4.0162	0.0560

4.2 Williamson-Hall analysis

The broadening of X-ray diffraction (XRD) peaks in nanocrystalline materials generally arises from two main factors: finite crystallite size and lattice strain[32]. To quantitatively distinguish these contributions, the Williamson–Hall (W–H) method was applied for $NiFe_{2-x}Al_xGd_xO_4$ thin films with compositions x= 0.00, 0.02, and 0.04 as shown in **Figure. 4**. The relation employed in the W–H approach is expressed as[33],

$$\beta \cos\theta = \frac{k\lambda}{t} + 4\varepsilon \sin\theta \qquad (9)$$

where β is the full width at half maximum (FWHM) of the diffraction peak (in radians), θ is the Bragg diffraction angle, k is the shape factor (taken as 0.9), λ is the wavelength of Cu–Kα radiation (1.5406 Å), D is the crystallite size, and ϵ is the lattice strain.

Plots of β cos θ against 4sin θ for all compositions exhibit a linear trend, confirming the validity of the W–H model. The intercept of the fitted line provides the inverse of the crystallite size, while the slope corresponds to the lattice strain[34]. The calculated crystallite sizes were found to decrease slightly with increasing Al^{3+} and Gd^{3+} co-doping, whereas the microstrain values showed a monotonic increase[35]. This behaviour suggests that the substitution of Fe^{3+} ions by larger Gd^{3+} and smaller Al^{3+} ions introduces local lattice distortions, thereby enhancing strain within the spinel framework[36].

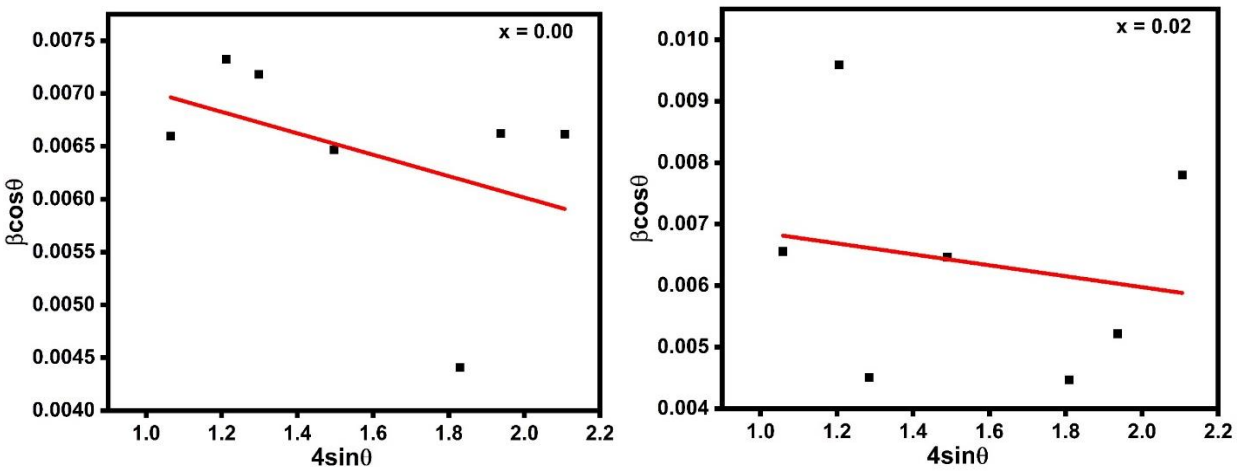

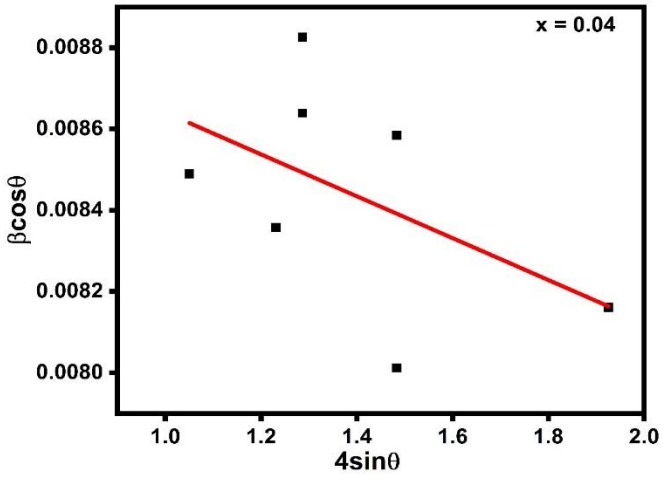

Figure 4. Williamson-Hall plot of $NiFe_{2-x}Al_xGd_xO_4$ (x = 0.00.0.02 and 0.04) thin films.

The results obtained from W–H analysis are consistent with the crystallite size trends predicted from the Scherrer equation. Still, they highlight the role of lattice strain in governing peak broadening. Thus, the co-doping of Al^{3+} and Gd^{3+} not only alters the crystallite growth mechanism but also introduces measurable distortions within the crystal lattice of nickel ferrite thin films.

4.3 Fourier Transform Infrared Spectroscopy

The Fourier Transform Infrared (FTIR) absorption spectra of the synthesised thin films, recorded in the frequency range of 400–4000 cm^{-1}, are presented in **Figure. 5** The spectra exhibit two characteristic absorption bands, one located near 600 cm^{-1} and the other around 400 cm^{-1}. These absorption features arise from lattice vibrations connected with the tetrahedral (A) and octahedral (B) sites of the spinel structure[37]. The higher-frequency band (ν_1), observed close to 600 cm^{-1}, corresponds to the stretching vibrations of metal–oxygen bonds at tetrahedral sites, while the lower-frequency band, appearing near 400 cm^{-1}, is attributed to metal–oxygen stretching at octahedral sites[38].

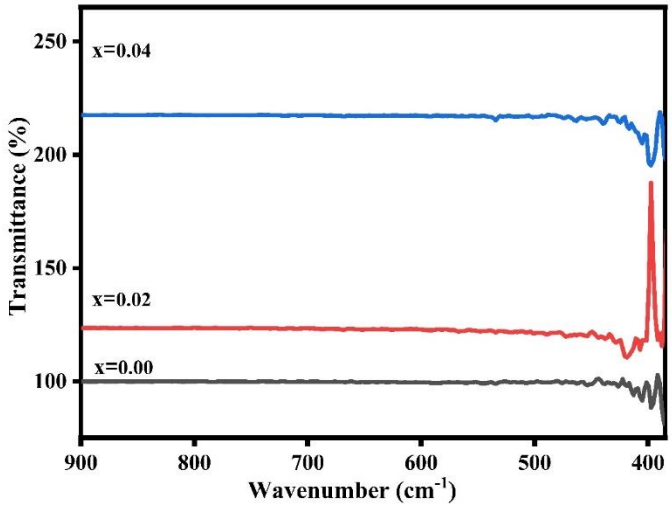

Figure. 5 FTIR spectra of $NiFe_{2-x}Al_xGd_xO_4$ (x = 0.00, 0.02 and 0.04) thin films

The positions of these bands for different Al^{3+} and Gd^{3+} concentrations are summarised in **Table. 5** Comparable absorption features have also been reported for other spinel ferrite systems, confirming the characteristic vibrational behaviour of the spinel lattice.

Table. 5 Values of absorption bands for the FT-IR spectrum of $NiFe_{2-x}Al_xGd_xO_4$ (x = 0.00, 0.02 and 0.04) thin films.

x	υ_1 cm^{-1}	υ_2 cm^{-1}
0.00	532	397
0.02	535	418
0.04	542	396
Attributed to	M-O	M-O

4.4 Current- Voltage (I-V) Characterisation

The current–voltage (I–V) characteristics of Al^{3+} and Gd^{3+} co-doped $NiFe_{2-x}Al_xGd_xO_4$ thin films deposited on glass substrates are shown in **Figure. 6** The curves exhibit a nearly linear relationship between current and applied voltage, confirming the formation of an ohmic contact between the electrodes and the films[39].

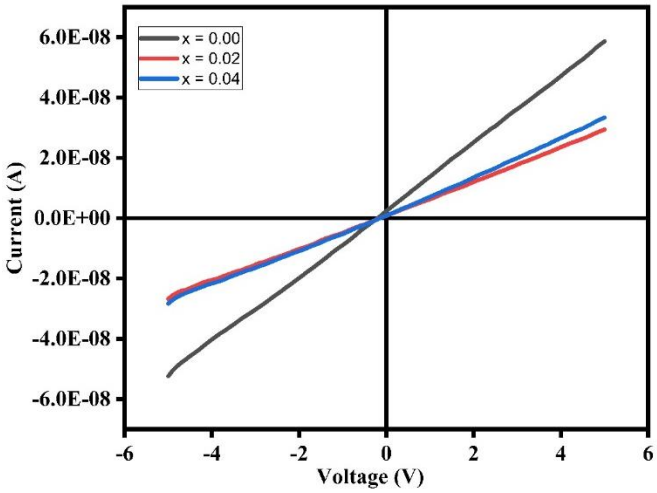

Figure 6. I-V curves of $NiFe_{2-x}Al_xGd_xO_4$ (x = 0.00, 0.02, and 0.04) thin films recorded at room temperature.

The thin films exhibit an ohmic nature, with resistance values in the order of mega ohms, and are listed in **Table. 5** Al^{3+} and Gd^{3+} co-doping strongly influences the resistivity of pure nickel ferrite. The I-V plots were used to calculate the resistivity of the films using the following relations[40].

$$\rho = \frac{RA}{t} \tag{10}$$

where, 'R' is the resistance, 'A' is the area of the thin film and 't' is the thickness of the thin film. The resistivity values are displayed in the table, which shows a decreasing trend with Al^{3+} and Gd^{3+} co-doping. The increase in resistivity can be attributed to 9.06×10^9 - 1.81×10^9 Ω-m, decreasing the concentration of

Al^{3+} and Gd^{3+} co-doping. This decrease in resistivity can be explained by the preferential tendency of Al^{3+} and Gd^{3+} to occupy either the A or B-site.

Table. 6 Resistivity of $NiFe_{2-x}Al_xGd_xO_4$ (x = 0.00, 0.02 and 0.04) thin films.

Composition x	**0.00**	**0.02**	**0.04**
Resistivity (Ω-m)	9.06	1.65	1.81

5. Conclusions

The deposited $NiFe_{2-x}Al_xGd_xO_4$ thin films exhibit a uniform thickness in the range of 239–257 nm and demonstrate a nanocrystalline nature. X-ray diffraction analysis confirms the formation of a single-phase cubic spinel structure. The average crystallite size, estimated using the Debye–Scherrer equation, lies between 9 and 15 nm. A systematic reduction in the lattice parameter is observed with the incorporation of Al^{3+} and Gd^{3+} ions, which can be attributed to the substitutional effect of the dopant ions. Fourier-transform infrared (FTIR) spectra reveal two distinct absorption bands corresponding to the metal–oxygen vibrations at tetrahedral and octahedral sites, further supporting the cubic spinel structure. Raman spectra exhibit the characteristic five active modes, namely T_2g (1), Eg, T_2g (2), T_2g (3), and A_1g (1), thereby confirming the spinel symmetry of the synthesized films. Current–voltage measurements at room temperature demonstrate nearly linear behaviour, indicating the formation of Ohmic contacts in the Al^{3+} and Gd^{3+} co-doped $NiFe_{2-x}Al_xGd_xO_4$ thin films.

Reference

1. Sambhudevan, S., *Ferrite-based polymer nanocomposites as shielding materials: A review.* Chemical Papers, 2021. **75**(8): p. 3697-3710.
2. Preethi, S., et al., *Unveiling the properties of layered 2D-based nano-material flexible electronics in biomedical applications: a review.* Journal of Materials Science, 2024. **59**(25): p. 11218-11245.
3. Anjum, S., et al., *Investigation of magnetic anisotropy in cobalt chromium (CoCr0. 5Fe1. 5O4) spinel ferrite thin films.* Journal of Superconductivity and Novel Magnetism, 2015. **28**(10): p. 3147-3156.
4. Pullar, R.C., *Hexagonal ferrites: a review of the synthesis, properties and applications of hexaferrite ceramics.* Progress in Materials Science, 2012. **57**(7): p. 1191-1334.
5. Amiri, M., M. Salavati-Niasari, and A. Akbari, *Magnetic nanocarriers: evolution of spinel ferrites for medical applications.* Advances in colloid and interface science, 2019. **265**: p. 29-44.
6. Prasad, S., et al., *Synthesis of MFe2O4 (M= Mg2+, Zn2+, Mn2+) spinel ferrites and their structural, elastic and electron magnetic resonance properties.* Ceramics International, 2018. **44**(9): p. 10517-10524.
7. Mustafa, G., et al., *Influence of the divalent and trivalent ions substitution on the structural and magnetic properties of Mg0. 5− xCdxCo0. 5Cr0. 04TbyFe1. 96− yO4 ferrites prepared by sol–gel method.* Journal of Magnetism and Magnetic Materials, 2015. **387**: p. 147-154.
8. Channagoudra, G., A.K. Saw, and V. Dayal, *Role of structure and cation distribution on magnetic and electrical properties in inverse spinel copper ferrite.* Journal of Physics and Chemistry of Solids, 2021. **154**: p. 110086.
9. Hussain, K., N. Amin, and M.I. Arshad, *Evaluation of structural, optical, dielectric, electrical, and magnetic properties of Ce3+ doped Cu0. 5Cd0. 25Co0. 25Fe2-xO4 spinel nano-ferrites.* Ceramics International, 2021. **47**(3): p. 3401-3410.
10. Shaikh, S.F., et al., *Types, synthesis methods and applications of ferrites*, in *Spinel Ferrite Nanostructures for Energy Storage Devices*. 2020, Elsevier. p. 51-82.
11. Hajalilou, A. and S.A. Mazlan, *A review on preparation techniques for synthesis of nanocrystalline soft magnetic ferrites and investigation on the effects of microstructure features on magnetic properties.* Applied Physics A, 2016. **122**(7): p. 680.

12. Sarveena, et al., *Wet Chemical Synthesis and Processing of Nanoferrites in Terms of Their Shape, Size and Physiochemical Properties*, in *Spinel Nanoferrites: Synthesis, Properties and Applications*. 2021, Springer. p. 63-84.
13. Hossain, I., et al., *Structural, morphological, optical and electrical properties of ferrite-based nanoparticles synthesized flexible substrate for chemical sensing application.* Journal of Science: Advanced Materials and Devices, 2024. **9**(3): p. 100750.
14. Sankapal, B.R., et al., *Simple chemical methods for thin film deposition.* Sankapal, BR, Gupta, RB, Ennaoui, A., Lokhande, CD, Eds, 2023.
15. Krebs, H.-U., et al., *Pulsed laser deposition (PLD)--a versatile thin film technique*, in *Advances in solid state physics*. 2003, Springer. p. 505-518.
16. Patil, D., V. Patil, and A. Jadhav, *Spray pyrolysis-based preparation and electrochemical study of zinc ferrite thin film.* Interactions, 2025. **246**(1): p. 1-14.
17. Kern, W. and K.K. Schuegraf, *Deposition technologies and applications: Introduction and overview*, in *Handbook of thin film deposition processes and techniques*. 2001, Elsevier. p. 11-43.
18. Hind, P.A., et al., *Influence of annealing on microstructure, nonlinear optical and electrical properties of spray pyrolyzed Sn0. 97La0. 03O2 films.* Optical Materials, 2022. **125**: p. 112080.
19. Dalawai, S.P., et al., *A review of spinel-type of ferrite thick film technology: fabrication and application.* Journal of Materials Science: Materials in Electronics, 2019. **30**(8): p. 7752-7779.
20. Jadhav, V.V., R.S. Mane, and P.V. Shinde, *Bismuth-ferrite-based electrochemical supercapacitors*. 2020: Springer.
21. Bouderbala, M., et al., *Thickness dependence of structural, electrical and optical behaviour of undoped ZnO thin films.* Physica B: Condensed Matter, 2008. **403**(18): p. 3326-3330.
22. Senthilkumar, S., *Development of Polymer based Controlled Drug Delivery Systems of Selected Antibacterial Agents*. 2014, The Tamilnadu Dr. MGR Medical University, Chennai.
23. Kurmude, D., et al., *X-ray diffraction and cation distribution studies in zinc-substituted nickel ferrite nanoparticles.* Journal of Superconductivity and Novel Magnetism, 2014. **27**(2): p. 547-553.
24. Sali, S., et al., *Nanocrystalline ZnO film deposited by ultrasonic spray on textured silicon substrate as an anti-reflection coating layer.* Physica B: Condensed Matter, 2012. **407**(13): p. 2626-2631.
25. Hussein, M.M., et al., *Impact of the Ni/Co ratio on structural and magnetic properties in A-site stoichiometric nanosized spinel ferrites.* Ceramics International, 2023. **49**(23): p. 39107-39116.
26. Rathod, S.V., et al., *Structural and optical characterization of Mg-doped nickel ferrite thin films.* Journal of Materials Science: Materials in Electronics, 2025. **36**(3): p. 191.
27. Shinde, P.G., et al., *Enhanced surface morphology, electrical and optical properties of ZnO thin film deposited by the doctor blade method.* Journal of Materials Science: Materials in Electronics, 2025. **36**(24): p. 1566.
28. Deshmukh, K.K., et al., *Impact of Mn2+-Ti4+ dopant on the photocatalytic dye degradation efficiency of Cobalt ferrite nanoparticle.* Ceramics International, 2025.
29. Lu, Y., et al., *Tailored strain–octahedral–defect interplay for giant multiferroicity in BiFeO3 via scandium implantation.* Journal of Materials Science & Technology, 2025.
30. Awan, T.I., S. Afsheen, and S. Kausar, *Emerging trends and issues related to thin films.* Thin Film Deposition Techniques: Thin Film Deposition Techniques and Its Applications in Different Fields, 2025: p. 241-278.
31. Li, Y., et al., *Tuning stacking fault energy and enhancing mechanical properties of Al through Mg and Sc doping: Insights from density functional theory.* Materials Today Communications, 2025. **43**: p. 111639.
32. Al-Tabbakh, A.A., et al., *Crystallite size and lattice strain of lithiated spinel material for rechargeable battery by X-ray diffraction peak-broadening analysis.* International Journal of Energy Research, 2019. **43**(5): p. 1903-1911.
33. Deshmukh, K.K., et al., *Role of tetravalent Ti4+ doping on the photocatalytic application of cobalt ferrite nanoparticles.* Materials Science and Engineering: B, 2026. **323**: p. 118807.
34. Bindu, P. and S. Thomas, *Estimation of lattice strain in ZnO nanoparticles: X-ray peak profile analysis.* Journal of Theoretical and Applied Physics, 2014. **8**(4): p. 123-134.

35. Raut, V.K., et al., *Sol-gel auto combustion synthesis of Al3+-Gd3+ ions co-doped cobalt ferrite nanoparticles for nanoelectronics applications.* Journal of Sol-Gel Science and Technology, 2024. **112**(3): p. 738-751.
36. Gopale, S.B., et al., *Influence of Al3+-Gd3+ co-substitution on the structural, morphological, magnetic and optical properties of nickel ferrite nanoparticles.* Journal of Materials Science: Materials in Electronics, 2022. **33**(35): p. 26544-26563.
37. Rathod, V., et al., *Correlated vibrations of the tetrahedral and octahedral complexes and splitting of the absorption bands in FTIR spectra of Li-Zn ferrites.* Vibrational Spectroscopy, 2017. **92**: p. 267-272.
38. Hossain, M., et al., *Properties Investigation of Mo-Substituted Ni-Zn Ferrites Using Solid-State Synthesis Techniques for High Frequency Applications.* Available at SSRN 5258884.
39. Chen, Q., S. Wang, and L.-M. Peng, *Establishing Ohmic contacts for in situ current–voltage characteristic measurements on acarbon nanotube inside the scanning electron microscope.* Nanotechnology, 2006. **17**(4): p. 1087.